



# Composition-Dependent Microstructure-Property Relationships of Fe and Al Modified Ti-12Cr (wt.%)

J. BALLOR<sup>1</sup>, M. IKEDA,<sup>2</sup> E.J. KAUTZ,<sup>3</sup> C.J. BOEHLERT,<sup>1,5</sup>  
and A. DEVARAJ<sup>4,6</sup>

1.—Department of Chemical Engineering and Materials Science, Michigan State University, East Lansing, MI, USA. 2.—Department of Chemistry and Materials Engineering Faculty of Chemistry, Materials and Bioengineering, Kansai University, 3-3-35, Yamate-cho, Osaka 564-8680, Japan. 3.—National Security Directorate, Pacific Northwest National Laboratory, Richland, WA, USA. 4.—Physical and Computational Sciences Directorate, Pacific Northwest National Laboratory, Richland, WA, USA. 5.—e-mail: boehlert@egr.msu.edu. 6.—e-mail: arun.devaraj@pnnl.gov

$\beta$ -Titanium (Ti) alloys have applications in several industries (e.g. aerospace, automotive, and biomedical) where material performance requirements vary widely. To tailor the microstructure and mechanical properties of  $\beta$ -Ti alloys for various applications, it is critical to understand the influence of individual alloying elements. Toward this goal, we investigated the effect of individual alloying additions on the microstructure and resultant mechanical properties of four model  $\beta$ -Ti alloys: Ti-12Cr, Ti-12Cr-3Al, Ti-12Cr-1Fe, and Ti-12Cr-1Fe-3Al (wt.%). The microstructures of these alloys were studied using x-ray diffraction, electron microscopy, and atom probe tomography. The mechanical properties were analyzed via Vickers and Rockwell hardness measurements and tensile testing. The addition of 1 wt.% Fe resulted in an approximate 5% increase in elongation-to-failure ( $\epsilon_f$ ), while the addition of 3 wt.% Al did not appear to significantly affect  $\epsilon_f$ . The addition of Fe and Al decreased the yield and ultimate tensile strengths.

## INTRODUCTION

$\beta$  Titanium ( $\beta$ -Ti) alloys are used in several industries, such as the aerospace, biomedical, chemical, and automotive industries, where high strength-to-weight ratios and corrosion resistance are desired.<sup>1–6</sup> The mechanical property requirements of components used in these industries vary. For example, biomedical applications require a low Young's modulus ( $E$ ) to prevent the stress-shielding of bone and promote healing,<sup>7</sup> while aerospace applications require high tensile strength and a range of elongation-to-failure ( $\epsilon_f$ ) values.<sup>3</sup> Processing can transform the metastable body-centered cubic (bcc)  $\beta$  phase into other metastable or equilibrium phases, affecting the mechanical properties. This allows the mechanical properties of  $\beta$ -Ti alloys to be tuned for specific applications. Recently, research into improving the mechanical properties of  $\beta$ -Ti alloys has been driven by the need to replace heavier automotive and aerospace components with lighter parts of equivalent or higher strength to

improve energy efficiency. This concept is known as "lightweighting." An example of lightweighting in aircraft is the replacement of 4.35 kg steel springs with springs made of Ti alloy Beta C that weigh 1.45 kg, as well as the replacement of fasteners with equivalent Beta C fasteners.<sup>3,4</sup> In the automotive industry, lightweighting of race cars using Ti alloys has been shown to improve performance.<sup>5</sup> However,  $\beta$ -Ti alloys usage in commercial automobiles is limited due to its higher cost in comparison to cheaper steel and aluminum alloys.<sup>5,8</sup>

One reason for the higher cost of Ti is its affinity for oxygen, nitrogen, hydrogen, and carbon. Because of this affinity, manufacturing processes to extract Ti metal from naturally occurring Ti oxides must be performed in a vacuum or inert gas, and most high-temperature processing leads to significant scale loss due to oxidation.<sup>9,10</sup> Subsequent processing of Ti into usable forms (such as bars, ingots, sheets, etc.) is also difficult, as are additional machining processes needed to manufacture usable Ti parts.<sup>8–10</sup>

One avenue to cut the cost of  $\beta$ -Ti is by changing the alloying elements from the relatively expensive and commonly used vanadium (V), niobium (Nb), and molybdenum (Mo) to low-cost alternatives.<sup>3</sup> Low-cost alternative alloying elements that provide equivalent  $\beta$ -phase stability can help lower the cost of the  $\beta$ -Ti alloys and make them more feasible for lightweighting applications. Before substitutions of low-cost alloying elements can be made, the impacts of such elements on the mechanical properties of the alloys must be identified. In this study, the composition-dependent, microstructure-property relationships of four low-cost Ti-chromium (Cr) alloys, with a homogenized microstructure, were studied and the contributions of the individual alloying elements on the microstructure and mechanical properties were determined.

### MATERIALS AND METHOD

Each alloy characterized in this study was levitation melted in a 2-kg, 90D $\times$ 80L LEV levitation induction furnace and hot forged at approximately 1320 K into 25  $\times$  60  $\times$  250-mm<sup>3</sup> blocks. After hot forging, the alloys were subjected to a homogenization anneal at 900°C for 1 h in vacuum. The alloys were then quenched in ice water at an estimated cooling rate of 34.7 K/s. This cooling rate was estimated in a similarly processed Ti-4.3Fe-7.1Cr-3.0Al (mass%). This high cooling rate is required to prevent  $\alpha$  phase formation.<sup>11</sup> The compositions of Cr, Fe, and Al in the manufactured alloys were determined by inductively coupled plasma atomic emission spectroscopy (ICP-AES) and the compositions of C, O, and N were determined using nondispersive infrared spectroscopy (NDIR) by the Daido Steel Corporation (Nagoya, Japan). The measured compositions of all the elements are provided in both wt.% and at.% in Table I, which shows that each alloy had approximately 12 wt.% Cr.

Samples for tensile testing were electrodischarge machine cut from the forged blocks into a “dogbone-shaped” geometry with a gauge length of 35 mm, width of 7  $\pm$  0.2 mm, and thickness of 1.1 mm.

Sample surfaces were polished using 320 grit silicon carbide paper and water to remove surface defects before tensile testing.

Conventional uniaxial tensile tests were performed using a MTS<sup>®</sup> servo-hydraulic testing machine equipped with an MTS<sup>®</sup> Flex Test SE controller. All tests were performed in an approximately 25°C air environment using a constant displacement rate of 0.025 mm/s, which corresponded to a strain rate of approximately 0.001 s<sup>-1</sup>. Strain was measured using an alumina-arm extensometer, with a 12-mm gauge length, spring-pressed to the side of the gage section.

In addition to uniaxial tensile testing, hardness testing was performed according to ASTM Standards E92-17 and E18-18a for Vickers microhardness and Rockwell B hardness, respectively. The undeformed regions of the tensile test samples (i.e., the grip sections) were used for hardness testing, and three separate samples for each alloy were used. Vickers microhardness testing was performed using a 500 g-force load and a dwell time of 15 s. Two Vickers microhardness measurements were taken for each sample for a total of 6 measurements per alloy. Nine total Rockwell B hardness measurements were taken, with three measurements taken on each sample.

Similarly, x-ray diffraction (XRD) was performed on the grip section of undeformed samples using a Scintag XDS 2000 Diffractometer in the Bragg-Brentano orientation. Cu-K <sub>$\alpha$</sub>  x-ray radiation, with a characteristic wavelength of 1.54 Å at 35-kV and 35-mA current, was used and the data were collected over a 2 $\theta$  range of 20° to 90°.

Back-scattered electron (BSE) images and energy-dispersive x-ray spectroscopy (EDS) measurements were taken using a FEI Quanta 3D field emission gun (FEG) dual beam focused ion beam/scanning electron microscope (FIB/SEM). Samples for SEM imaging were cut from the forged alloy blocks using a diamond saw. The samples were mounted in a conductive resin and metallographically polished to a mirror finish according to Ref. 12. The final polish included a 50/50 mixture of Struers

**Table I. Measured compositions of the Ti-Cr-Fe-Al alloys characterized in this work**

| Alloy                  |      | Chemical composition |      |      |      |       |       |       |
|------------------------|------|----------------------|------|------|------|-------|-------|-------|
|                        |      | Ti                   | Cr   | Fe   | Al   | C     | O     | N     |
| Ti-12Cr (TC)           | wt.% | Bal.                 | 12.1 | 0.02 | 0.01 | 0.004 | 0.059 | 0.004 |
|                        | at.% | Bal.                 | 11.2 | 0.02 | 0.02 | 0.02  | 0.18  | 0.01  |
| Ti-12Cr-3Al (TCA)      | wt.% | Bal.                 | 12.3 | 0.02 | 3.06 | 0.003 | 0.062 | 0.004 |
|                        | at.% | Bal.                 | 11.2 | 0.02 | 5.35 | 0.01  | 0.18  | 0.01  |
| Ti-12Cr-1Fe (TCF)      | wt.% | Bal.                 | 12.5 | 0.93 | 0.02 | 0.003 | 0.069 | 0.004 |
|                        | at.% | Bal.                 | 11.6 | 0.80 | 0.04 | 0.01  | 0.21  | 0.01  |
| Ti-12Cr-1Fe-3Al (TCFA) | wt.% | Bal.                 | 12.4 | 0.93 | 3.02 | 0.003 | 0.11  | 0.004 |
|                        | at.% | Bal.                 | 11.3 | 0.79 | 5.28 | 0.01  | 0.32  | 0.01  |

OP-S Colloidal silica (0.02–0.04 micron) and 30% hydrogen peroxide. After polishing, the samples were etched using Kroll's reagent (2-mL HF, 6-mL nitric acid, 92-mL distilled water).

Needle specimens for atom probe tomography (APT) were prepared from the polished bulk metallographic samples by the focused ion beam (FIB)-based lift-out and annular milling method described in Ref. 13. The FEI Quanta 3D FEG dual beam FIB/SEM used for backscattered electron (BSE) imaging, which was equipped with an Omniprobe nanomanipulator, was also used for the APT sample preparation. A CAMECA local electrode atom probe (LEAP) 4000X HR system was used for all APT data collection, with the following user-selected parameters in pulsed-voltage mode: 200-kHz pulse frequency, 20% pulse fraction, 55 K specimen temperature, and 0.005 atoms/pulse detection rate. All data sets were reconstructed and analyzed using the Interactive Visualization and Analysis Software (IVAS) version 3.8.2.

## RESULTS AND DISCUSSION

### Microstructure Characterization

XRD scans of each of the as-processed alloys revealed peaks corresponding to the  $\beta$  phase (see Fig. 1). The TCA alloy exhibited a larger (211)  $\beta$  peak compared to the other alloys. This texturing could be from the addition of Al. Slight shifts of the  $\beta$  peak locations, likely due to the difference in the atomic radii of Ti, Cr, Fe, and Al, were observed.

Bragg's Law, provided in Eq. 1, was used to evaluate how the alloying additions affected the lattice parameter ( $a$ ).

$$\lambda = 2 \times d \times \sin(\theta) \quad (1)$$

$d$  was the spacing between the (200) planes,  $\lambda$  was the monochromatic x-ray wavelength corresponding to Cu-K $\alpha$  radiation (1.54 Å), and  $\theta$  was the angle at which the x-ray was incident on the sample. Table II lists the calculated lattice parameters, calculated to be  $2d$ . The estimated error associated with the  $2\theta$  peak location for these measurements was 0.5°, leading to the  $\pm 0.2$  Å error for each calculated lattice parameter.

The room-temperature (RT)  $\beta$ -phase lattice parameter is purely a theoretical value because the  $\beta$  phase is not an equilibrium phase in pure Ti at RT.<sup>10</sup> Both the additions of Cr and Fe and the additions of Cr and Al resulted in a decrease of the lattice parameter beyond the range of error. Cr, Fe, and Al all have smaller radii than Ti; therefore, this result is not surprising. Although the addition of Cr and the addition of Cr and Fe and Al decreased the lattice parameter, this decrease was not beyond the range of error. Overall, the changes in the lattice parameter were small. However, even small lattice strains, introduced due to alloying, can affect hardness,  $E$ ,  $\epsilon_f$ , and strength.

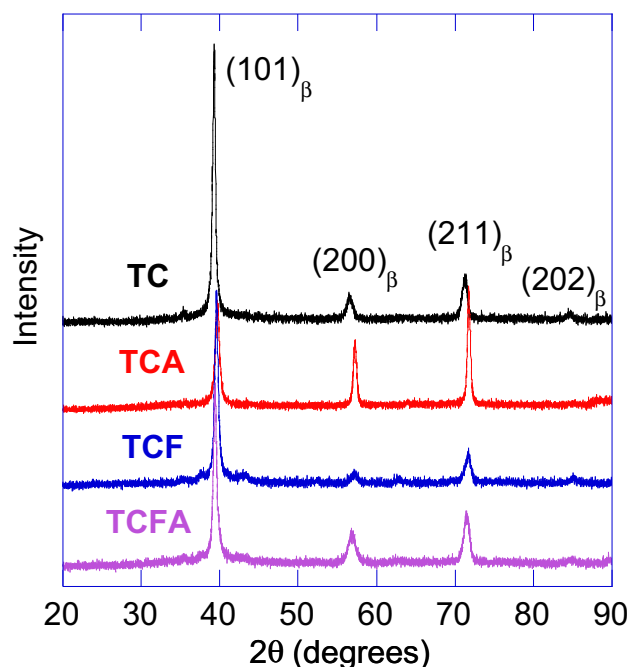


Fig. 1. XRD scans of the TC, TCA, TCF, and TCFA alloys, showing the (101), (200), (211), and (202)  $\beta$  peaks.

Table II. Calculated lattice parameters of Each  $\beta$ -Ti alloy

| Alloy    | Lattice parameter (Å) |
|----------|-----------------------|
| Pure Ti* | $3.282 \pm 0.003$     |
| TC       | $3.26 \pm 0.2$        |
| TCA      | $3.22 \pm 0.2$        |
| TCF      | $3.22 \pm 0.2$        |
| TCFA     | $3.24 \pm 0.2$        |

\*Theoretical value from Ref. 12.

The forged blocks were evaluated in three different orientations for each alloy in order to estimate the average  $\beta$  phase grain size and to identify the presence of secondary phases; the alloys were carefully characterized in three orientations referred to as cross section, thickness, and top; see supplementary Fig. S1 (refer to online supplementary material). The  $\alpha$ -phase rejects  $\beta$ -stabilizing elements, such as Cr and Fe, during precipitation and growth,<sup>14</sup> leading to regions of different elemental composition, which can be identifiable using BSE imaging. Thus, high-magnification BSE imaging was used to help identify the  $\alpha$  phase within the  $\beta$  phase or along the  $\beta$ -phase grain boundaries. Although the  $\alpha$  phase was identified at the very edges of the forgings, which was likely due to the higher O contents at such locations, no  $\alpha$  phase was identified either along  $\beta$  grain boundaries or at the grain interiors in the bulk of any of the alloys.

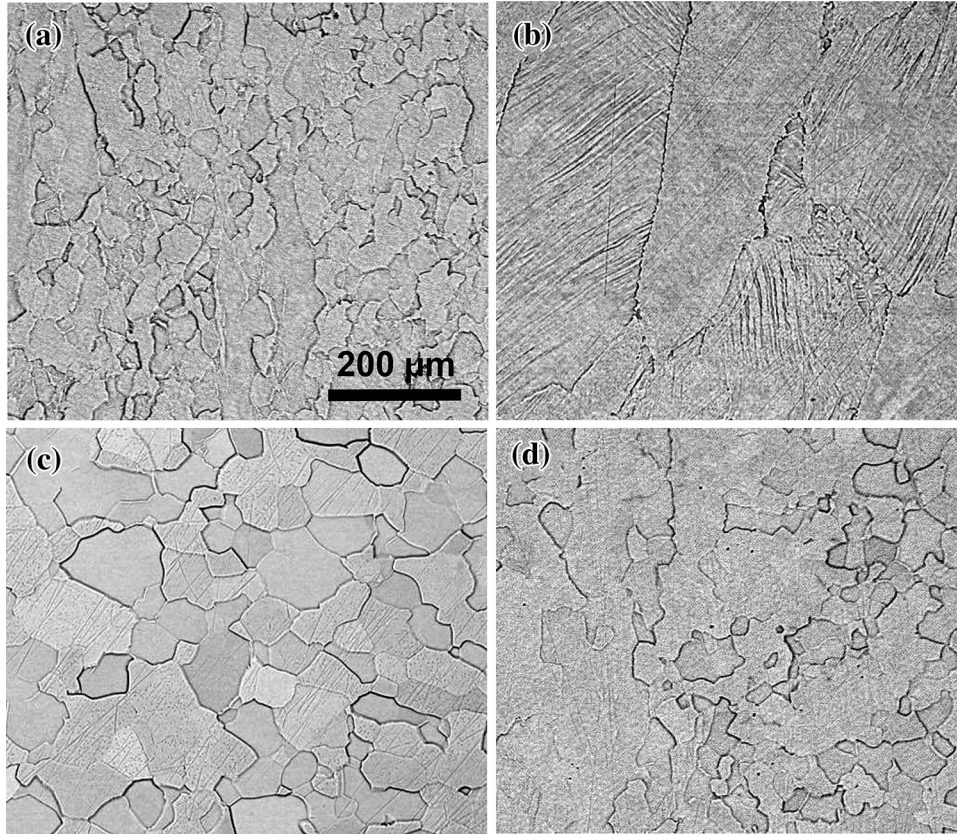


Fig. 2. Representative BSE SEM photomicrographs of the cross section of the (a) TC, (b) TCA, (c) TCF, and (d) TCFA alloys.

Transmission electron microscopy analysis is currently in progress to unequivocally confirm the phases present in these alloys and will be the subject of a future publication. Figure 2 shows representative BSE images of all the alloys. While Fig. 2b has plate- or needle-shaped lamella in the microstructure, these features are an artifact of the etching process. EDS measurements taken of the lamella (see supplementary Fig. S2) indicate that the lamella are surface features, not a different phase. It is noted that because all the edges were polished away during the sample preparation, no  $\alpha$  phase was present in any of the samples characterized for the mechanical properties.

The  $\beta$ -phase grain sizes were measured for each orientation according to the method detailed in ASTM standard E112-12.<sup>15</sup> Three images, with one taken at each of the following magnifications: 120 $\times$ , 200 $\times$ , and 500 $\times$ , were used to measure the grain size. Procedures for measuring the intercept length, outlined in section 16.3 of ASTM E112-12, were used with the randomly placed test line method. For example, the mean lineal intercept lengths ( $\bar{l}$ ) were calculated from the total test line length ( $L$ ), the magnification of the image ( $M$ ), and the total number of intersections ( $N$ ) according to Eq. 2 (developed from equations 10 and 12 in ASTM E112-12):<sup>15</sup>

$$\bar{l} = \bar{N}_L^{-1} = \frac{L/M}{N} \quad (2)$$

and the corresponding values are provided for each orientation in Table III. To calculate the overall mean lineal intercept length, reported as “Overall Mean” in Table III, the average  $\bar{N}_L$  was calculated as such:

$$\bar{N} = (\bar{N}_{L\text{thickness}} * \bar{N}_{L\text{top}} * \bar{N}_{L\text{cross-section}})^{1/3} \quad (3)$$

The average  $\bar{N}$  was used to calculate the grain size number, also reported in Table III, according to ASTM E112.<sup>15</sup>

Adding Fe or Al resulted in an increased grain size in all three orientations. The addition of Fe approximately doubled the average grain size. The addition of Al nearly tripled the average grain size; thus, Al had a more pronounced effect on enhancing the grain size. However, when Al was added to the TCF alloy, the average grain size only increased by 20%. As such, there appears to be a reduced effect of Al on grain growth when combined with Fe addition. Overall, by adding both 3 wt.% Al and 1 wt.% Fe to Ti-12Cr (wt.%), a greater than doubling of the average grain size resulted.

Even though an  $\alpha$  stabilizing element (Al) was included in two of the alloys (TCA and TCFA), the presence of 12 wt.% Cr (a  $\beta$  stabilizing element)

**Table III. Summary of the measured grain sizes for the four alloys studied**

| Orientation                                 | TC   | TCA   | TCF  | TCFA |
|---|------|-------|------|------|
| $\bar{l}$ , Cross-section ( $\mu\text{m}$ ) | 33.9 | 84.0  | 50.9 | 57   |
| $\bar{l}$ , Top ( $\mu\text{m}$ )           | 46.0 | 134.2 | 86.8 | 78.4 |
| $\bar{l}$ , Thickness ( $\mu\text{m}$ )     | 27.1 | 94.2  | 52.3 | 89.1 |
| Overall mean ( $\mu\text{m}$ )              | 34.9 | 102.0 | 61.3 | 73.6 |
| Grain size number ( $G$ )                   | 6.4  | 3.3   | 4.8  | 4.2  |

appears to have suppressed the  $\alpha$  phase formation in all four alloys. This observation was confirmed by the SEM and XRD results. Thereby any influence of a second phase on the mechanical properties was eliminated, and both solid solution strengthening and grain size were expected to have the greatest influence on the hardness values and tensile properties.

Although the contrast in the BSE images did not indicate any clear elemental partitioning in the  $\beta$  phase in any of the alloys, potential partitioning could still not be ruled out because the relatively large interaction volume of the 30-keV electron beam limits the sensitivity of image contrast to compositional fluctuations above  $1\ \mu\text{m}$ .<sup>16</sup> However, nanoscale  $\alpha$ -phase precipitation, which could not be resolved in SEM BSE images, has been reported in some other  $\beta$ -Ti alloys depending on the specific thermomechanical treatments.<sup>17</sup> If such nanoscale  $\alpha$ -phase precipitation occurred in any of the four alloys studied here, it should induce a nanoscale compositional partitioning. Hence, to check this nanoscale compositional homogeneity of all four alloys, APT analysis was conducted.

The APT results, provided in Fig. 3, show Ti, Cr, Al, and Fe element distributions in all four alloys. Table IV shows the comparison of the measured composition of all four alloys from APT reconstructions, SEM-EDS analysis, and ICP-AES methods.

The Cr concentrations of the alloys measured from APT are approximately 2% to 3% higher than the bulk Cr concentrations reported by Daido Steel. The concentrations of Al in the TCA and TCFA alloys differ, with the TCA alloy containing approximately 0.36 at.% more Al than the reported bulk concentration, and the TCFA alloy containing approximately 0.8 at.% less. Higher amounts of C were also measured in the APT tips than in the bulk. Gallium, which is sometimes implanted during the FIB/SEM lift-out process, was only present at concentrations of less than 0.07% in all the data sets used for this study.

The EDS measured concentration of Ti, Cr, Fe, and Al in all alloys was lower than the bulk and APT measurements. While EDS is not sensitive to light elements such as C and O, it is noted that the EDS measured concentrations of C and O were significantly higher than the bulk measurements in all alloys except TC, where O was measured to be

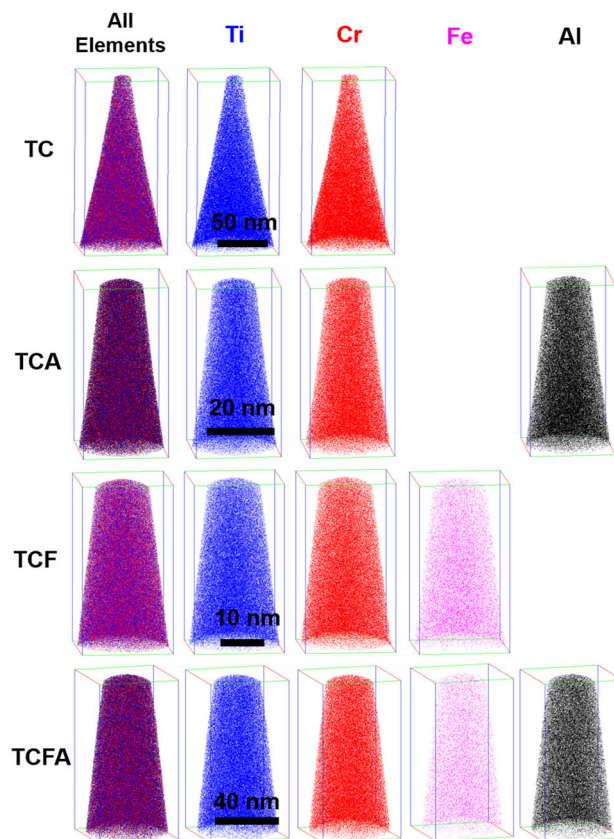


Fig. 3. Element distribution maps for the TCFA alloys. The all ionic view of the APT reconstruction is shown on the far left, in addition to the labeled Ti, Cr, Fe, and Al ion maps, all showing a uniform distribution of ions. The element distribution maps shown here are representative of all samples studied in this work, and the same uniform ion distribution was observed in all alloys.

0 at.%. The C at.% determined via SEM-EDS is significantly higher than that measured via ICP-AES or APT, most likely due to C-contamination on sample surfaces. EDS would include surface C in the overall concentration measurement, while the bulk measurement would not. APT sample preparation involves a removal of the ion-beam damaged surface during a final polishing step, which would also remove this surface C, which can explain the lower measured C in the APT concentration measurements.

The ICP-AES and NDIR analysis of all the alloys, provided in Table I, did not estimate the dissolved H concentration in these alloys. For a direct comparison between the average bulk concentration of alloys obtained from ICP-AES and NDIR analysis and the APT measured composition, the APT results in Table IV were also calculated without including hydrogen (H) in the analysis. However, there are recent studies that suggest H could be introduced into APT samples through Ga ion irradiation during the FIB lift-out process when performed at room temperature. Furthermore, H in mass spectra could also be attributed to residual H in the APT analysis

**Table IV. Alloy composition measured via APT, with  $\pm 1$  standard deviation, compared with composition measured via ICP-AES and SEM-EDS**

| Alloy | Method           | Ti (at.%)      | Cr (at.%)       | Fe (at.%)        | Al (at.%)       | C (at.%)        | O (at.%)        | N (at.%)         |
|-------|------------------|----------------|-----------------|------------------|-----------------|-----------------|-----------------|------------------|
| TC    | APT              | $84.7 \pm 1.1$ | $14.1 \pm 1.3$  | $0.03 \pm 0.005$ | 0.01*           | $0.91 \pm 0.31$ | $0.21 \pm 0.04$ | $0.02 \pm 0.02$  |
|       | ICP-AES and NDIR | 88.5           | 11.2            | 0.02             | 0.02            | 0.02            | 0.18            | 0.01             |
|       | EDS              | 73.33          | 10.58           | 0.04             | 0               | 16.05           | 0               | 0                |
| TCA   | APT              | $79.7 \pm 0.2$ | $13.7 \pm 0.1$  | $0.04 \pm 0.02$  | $5.71 \pm 0.26$ | $0.49 \pm 0.09$ | $0.23 \pm 0.03$ | $0.13 \pm 0.13$  |
|       | ICP-AES and NDIR | 83.3           | 11.2            | 0.02             | 5.35            | 0.01            | 0.18            | 0.01             |
|       | EDS              | 63.7           | 9.36            | 0.03             | 3.77            | 13.55           | 9.6             | 0                |
| TCF   | APT              | $83.9 \pm 0.1$ | $14.0 \pm 0.05$ | $0.94 \pm 0.11$  | $0.08 \pm 0.04$ | $0.68 \pm 0.08$ | $0.32 \pm 0.05$ | $0.03 \pm 0.001$ |
|       | ICP-AES and NDIR | 87.3           | 11.6            | 0.8              | 0.04            | 0.01            | 0.21            | 0.01             |
|       | EDS              | 65.81          | 9.44            | 0.71             | 0               | 13.66           | 10.38           | 0                |
| TCFA  | APT              | $79.0 \pm 1.1$ | $13.3 \pm 0.14$ | $1.10 \pm 0.16$  | $4.48 \pm 1.39$ | $0.85 \pm 0.54$ | $0.32 \pm 0.05$ | $0.93 \pm 0.79$  |
|       | ICP-AES and NDIR | 82.3           | 11.3            | 0.79             | 5.28            | 0.01            | 0.32            | 0.01             |
|       | EDS              | 62.24          | 9.08            | 0.69             | 3.66            | 11.48           | 12.86           | 0                |

All SEM-EDS measurements were taken from a sample area of approximately  $1200 \mu\text{m} \times 1200 \mu\text{m}$  (see supplementary Fig. S3 for an example region from which the EDS measurement was taken).

chamber.<sup>18,19</sup> Given these recent developments, a supplementary Table S-I, including the H concentration measured from APT for all the data sets, is provided to report the H content in the mass spectra analyzed, and to compare the compositions of Ti alloys when H is taken into account. The APT results from the TC and TCFA alloys contained the highest average concentrations of H, at 15.4% and 32.7%, respectively, while the APT results from the TCA and TCF alloys contained between 2% and 4% average H. The sample preparation procedure was the same for all samples, with the exception of the accelerating voltage during deposition of the electron beam assisted platinum cap at the start of the lift out procedure. For the TC and TCFA alloys, an electron beam accelerating voltage of 30 kV was used, while 5 kV was used for the TCA and TCF alloys.

The ion maps in Fig. 3 indicate that the element distribution in all four alloys was relatively uniform. To check for local elemental ordering/clustering in these alloys, a frequency distribution analysis was performed using 100 atom bins,<sup>20</sup> the results of which are shown in Fig. 4. For a homogenous solid solution, the observed frequency distribution should match a calculated binomial distribution.<sup>21</sup> Looking at the observed and the binomial frequency distributions, all observed measurements seem to match well to the binomial distributions, suggesting that the compositions are relatively homogenous in the volumes analyzed via APT. The largest visible difference in the observed and binomial distributions is in the Ti distribution of the TC alloy, suggesting ordering/clustering of the Ti atoms.

To quantitatively evaluate the distributions, Pearson correlation coefficients ( $\mu$ ) were calculated, which measure deviance from a random solid solution.<sup>22,23</sup>  $\mu$  was used instead of a  $\chi^2$  value because  $\mu$  can be used to directly compare ordering/clustering between data sets of different sizes.<sup>21,24</sup> A  $\mu$  equal to 0 indicates a binomial distribution of the atoms, while a  $\mu$  equal to 1 indicates complete association between the chosen atoms.<sup>24</sup> Agreeing with the observation that the observed Ti distribution is nonrandom, in the TC alloy, the calculated  $\mu$  for Ti in TC was the highest for Ti in all alloys, with a value of 0.265. This  $\mu$  value suggests that Ti is distributed relatively nonuniformly in the TC alloy, which could affect the mechanical properties of the alloy. While other smaller deviations are visible in the frequency distributions in the TCA, TCF, and TCFA alloys,  $\mu$  was  $< 0.1$  for all other distributions, indicating a closer to ideal homogenous distribution in those alloys.

While the element distribution maps can provide qualitative visual information regarding any nanoscale partitioning of the elements, and the frequency distribution analysis gives quantitative information on overall compositional segregation, radial distribution function (RDF) analysis can provide information on the spatial relationships of atoms.<sup>20</sup> RDF analysis provides information on the local neighborhood of the specified atoms in a radial direction, which allows for the determination of local ordering/clustering that other techniques cannot identify. RDFs for each alloy were created with respect to the ions from the  $\text{Ti}^{2+}$  peak at 24 Daltons (Da). This peak was selected because there was no overlap with other peaks in the Ti-Cr-Fe-Al alloy mass

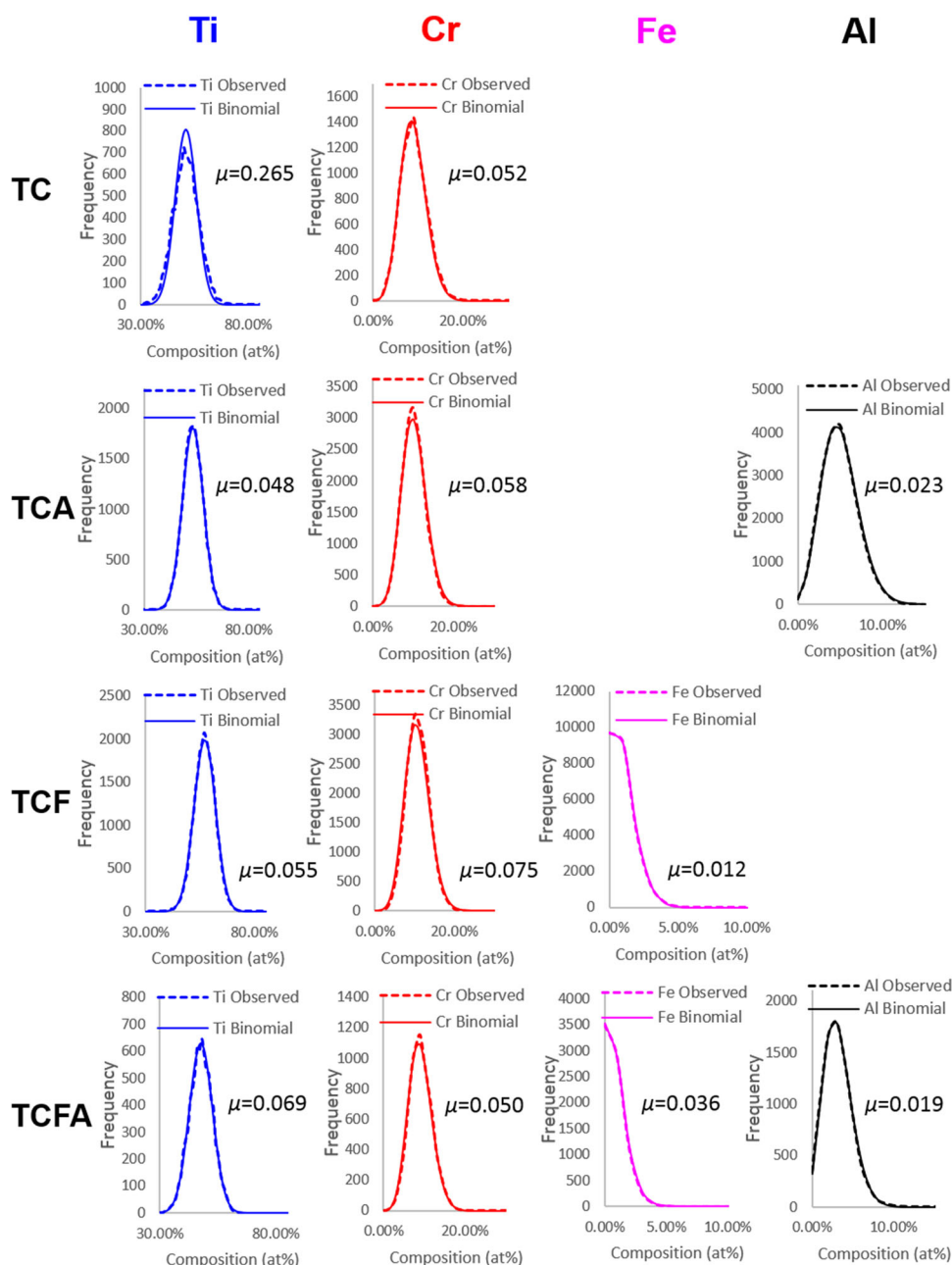


Fig. 4. Elemental frequency distribution maps for the TCFA alloys. These maps are representative of all samples studied and include the  $\mu$  of each distribution.

spectrum. Similarly, the 26 Da  $\text{Cr}^{2+}$ , 28 Da  $\text{Fe}^{2+}$ , and 13.5 Da  $\text{Al}^{2+}$  peaks were used in the analysis. The shell thickness for RDF was kept at 0.1 nm, and RDF analysis was conducted for a maximum distance of 2 nm from the center Ti atoms. The RDFs were then normalized with the bulk concentration of each alloy to obtain the bulk normalized concentration shown in Fig. 5.

When the bulk normalized concentration of two atoms are greater than 1, there is a positive correlation, while a value of 1 indicates no correlation, and a value less than 1 means anti-correlation. At distances greater than 0.5 nm, the RDFs settle

into constant values close to 1 for all alloys. However, within the first 0.5 nm, specific correlation trends are observed between center Ti atoms and all the other elements in all four alloys. All four alloys show that Ti had a positive correlation with Cr. Ti also shows a slight positive correlation for other Ti atoms in the TC alloy. Fe has an anti-correlation with Ti in the TCF and TCFA alloys, particularly in the TCFA alloy at distances close to the Ti atom, but it steadily rises, going from less than one to greater than one as the distance increases. Al also appears to have anti-correlation in the TCA and the TCFA alloys, with bulk

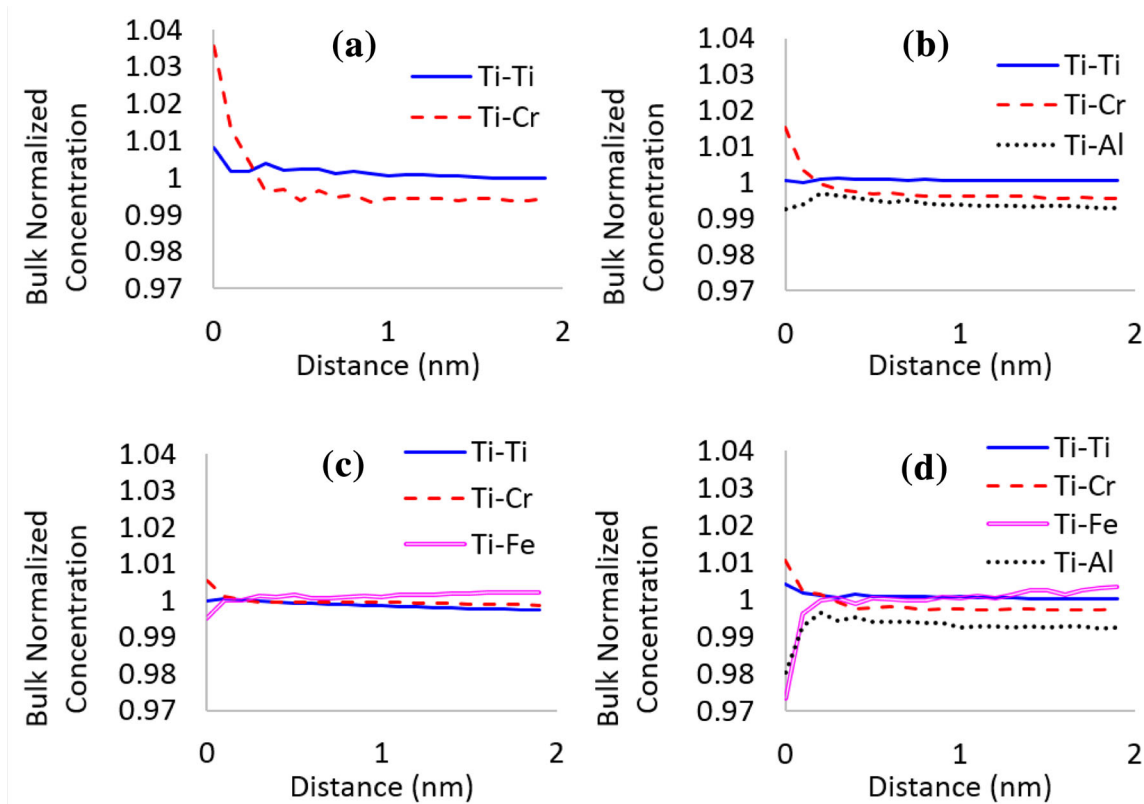


Fig. 5. Radial distribution functions of elemental concentrations in the (a) TC, (b) TCA, (c) TCF, and (d) TCFA alloys.

normalized concentration being less than one in both alloys.

### Mechanical Properties

Vickers hardness and Rockwell hardness were used to test the hardness of the alloys, and the results are shown in Fig. 6a and b. No significant difference in the hardness values were exhibited by the alloys. The apparent drop in the Vickers microhardness exhibited by the TCA alloy was determined to not be significant since it was not reflected in the Rockwell B hardness results. Thus, the addition of Al and/or Fe did not appear to significantly affect the hardness of Ti-12Cr.

The RT stress-strain curves illustrated in Fig. 7 indicate that the  $\varepsilon_f$  values were similar for TC and TCA, while both  $\varepsilon_f$  values were significantly less than those for TCF and the TCFA, with TCFA exhibiting the highest  $\varepsilon_f$  (11.7%). It is noted that only one tensile specimen from each alloy was tested. The E, 0.2% proof strength ( $\sigma_y$ ), ultimate tensile strength (UTS), and  $\varepsilon_f$  are listed in Table V. The 0.2% proof strength, UTS, and  $\varepsilon_f$  were calculated using sections 7.7.1, 7.10, and 7.11.5 of ASTM standard E8-E8M-13a, respectively.

The E values were similar; however, TC exhibited the highest 0.2% proof strength and UTS. The TCA and TCF alloys exhibited similar UTS values, which were lower than the other two alloys. These results suggest that the addition of either Al or Fe alone to

Ti-12 wt.%Cr marginally lowers both the 0.2% proof strength and UTS. However, the addition of both 1 wt.% Fe and 3 wt.% Al resulted in strengths closer to TC.

Comparing the 6.0%  $\varepsilon_f$  of TC to the 10.5%  $\varepsilon_f$  of TCF shows that the addition of just 1 wt.% Fe increased the  $\varepsilon_f$  of the alloy by 4.5%. The large increase in  $\varepsilon_f$  due to 1 wt.% Fe additions indicates that Fe addition increases the  $\varepsilon_f$  of Ti-12 wt.% Cr alloys. However, the addition of 3 wt.% Al to TC resulted in an  $\varepsilon_f$  of 6.2%, which was almost identical to that for TC. The TCFA alloy demonstrated the highest  $\varepsilon_f$  value (11.7%), which is an increase of 5.5% strain in comparison to that for TC.

From the BSE images in Fig. 2 and the grain sizes measured in Table III, it is clear that the grain size change brought about by addition of Al and/or Fe to TC cannot directly explain the observed difference in the hardness and tensile properties. For example, TC and TCA exhibited the lowest and highest grain sizes, respectively, and interestingly they exhibited similar  $\varepsilon_f$  values. One possibility of how Fe increases the  $\varepsilon_f$  of the alloys is through the deformation mode. Fe is a strong  $\beta$  stabilizer, and the  $\beta$  stability affects the deformation modes in  $\beta$  alloys. As  $\beta$  stability increases, the dominant deformation mode changes from a primarily martensitic transformation to a combination of twinning and deformation-induced omega phase formation, then to only twinning, and finally to slip-based deformation in the most



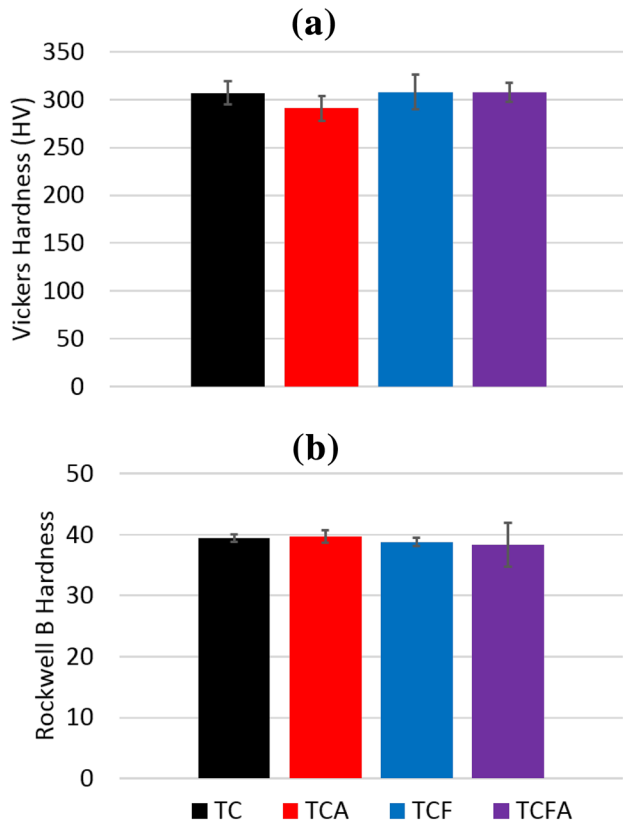


Fig. 6. Average (a) Vickers microhardness values and (b) Rockwell B hardness values measured for each alloy. The error bars show  $\pm 1$  standard deviation from the average.

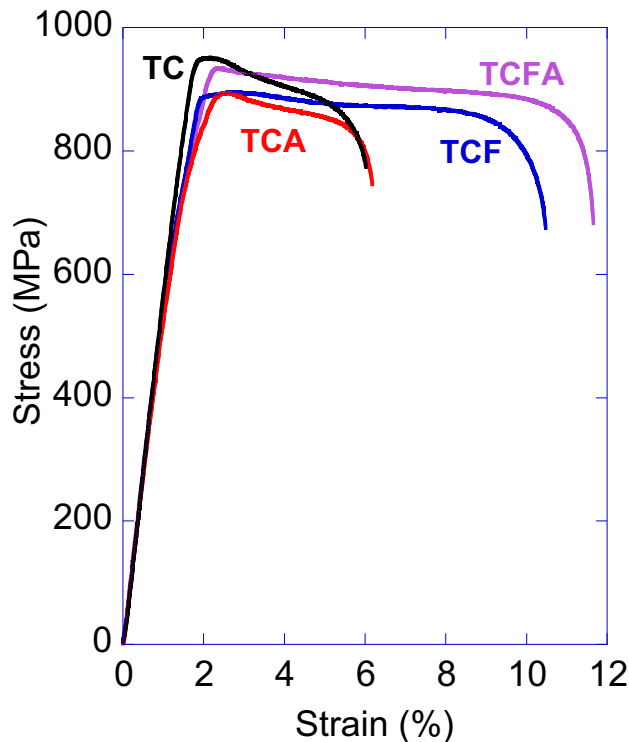


Fig. 7. RT tensile engineering stress versus engineering strain curves of the TC, TCA, TCF, and TCFA alloys. All tests were conducted to failure.

Table V. Summary of the tensile properties for each alloy

| Alloy | E (GPa) | $\sigma_y$ (MPa) | UTS (MPa) | $\epsilon_f$ (%) |
|-------|---------|------------------|-----------|------------------|
| TC    | 58      | 941              | 951       | 6.0              |
| TCA   | 54      | 770              | 895       | 6.2              |
| TCF   | 56      | 780              | 895       | 10.5             |
| TCFA  | 56      | 776              | 935       | 11.7             |

stable  $\beta$ -Ti alloys.<sup>25–30</sup> The deformation mode affects the  $\epsilon_f$  of  $\beta$ -Ti alloys, with twinning providing higher  $\epsilon_f$  than slip.<sup>26</sup> In a study on  $\beta$ -stability and the corresponding mechanical properties, Hanada and Izumi<sup>26</sup> found that Ti-20V-3Sn (wt.%) exhibited the highest  $\epsilon_f$  (39%) when only the twinning deformation mode was activated, but adding 6Al (wt.%) instead of 3Sn (wt.%) to Ti-20V (wt.%) activated the slip deformation mode instead, and a lower  $\epsilon_f$  (14%) was exhibited. Analysis of the deformation and fracture of the samples is necessary to more thoroughly determine the effect of Fe on  $\epsilon_f$ , which will be the subject of future work.

The observation of the positive correlation between Ti-Cr and the anti-correlation between Ti-Fe and Ti-Al from the APT results indicates local ordering tendencies between these elements. The magnitude of maximum bulk normalized concentration between Ti-Cr reduced from 1.04 to 1.02 with addition of Al, and it was further reduced to 1.01 with addition of Fe and Al. This indicates that the TC alloy might show the highest local ordering tendency, while the lowest ordering between Ti-Cr was in the TCFA alloy. These results, at least qualitatively, can help explain why the TC alloy exhibited the highest UTS and the lowest  $\epsilon_f$ . Such local ordering tendencies can introduce anisotropic lattice distortion in the  $\beta$  phase, which then can affect the dislocations and/or twinning based deformation mechanisms. Detailed analysis of deformed microstructures of these alloys may provide further information on such mechanisms and provide a new approach to tailor the  $\beta$ -Ti alloy composition, which is also a subject of our ongoing studies.

### SUMMARY AND CONCLUSION

Mechanical properties, particularly hardness, E,  $\epsilon_f$ ,  $\sigma_y$ , and UTS, of  $\beta$ -Ti alloys can be affected by modifying the alloy chemistry. The effects of minor Fe and Al additions (1 and 3 wt.%, respectively) on the microstructure and mechanical properties of a Ti-12Cr (wt.%)  $\beta$  alloy were investigated in this work.

XRD, SEM, EDS and APT results confirmed that all alloys were fully  $\beta$  stabilized. The results indicated that any measurable mechanical property differences resulted from minor alloying element additions and their ordering tendencies, rather than from the presence of a secondary phase. Grain size

measurements showed that adding Fe or Al to the base Ti-12Cr alloy increased the average grain size, whereas Al additions led to a higher average grain size than Fe.

The addition of Al and/or Fe did not affect the hardness or E of the alloys. The  $\sigma_y$  and UTS were lower in the alloys containing just Al, just Fe, or both Al and Fe. The alloys containing just Al addition or just Fe additions exhibited the lowest strengths. The addition of Al and Fe lowered the tensile strength of Ti-12Cr.

Adding 1 wt.% Fe increased the  $\varepsilon_f$  of the TC alloy by 4.5%, and adding 1 wt.% Fe increased the  $\varepsilon_f$  of the TCA alloy by 5.5%. The addition of only Al was shown to not significantly affect the  $\varepsilon_f$  values.

Such systematic studies using binary, ternary, and quaternary model alloys are crucial to the improved understanding of microstructure-property relationships and the role of alloy chemistry.

### ACKNOWLEDGEMENTS

This material is based in part on work supported by the U.S. Department of Energy, Office of Science, Office of Workforce Development for Teachers and Scientists, Office of Science Graduate Student Research (SCGSR) program. The SCGSR program is administered by the Oak Ridge Institute for Science and Education for the DOE under contract number DE-SC0014664. The funding for the alloy processing, mechanical testing metallographic preparation and XRD was supported by National Science Foundation Division of Material Research (Grant No. DMR1607942) through the Metals and Metallic Nanostructures (MMN) program. A.D. would like to acknowledge the funding support from Pacific Northwest National Laboratories laboratory directed research and development (LDRD) program as a part of physical and computational sciences directorate seed LDRD. The microstructural characterization using SEM and APT was performed using facilities at the Environmental Molecular Sciences Laboratory, a national scientific user facility sponsored by the Department of Energy's Office of Biological and Environmental Research and located at Pacific Northwest National Laboratory. The authors also acknowledge the assistance of Ms. Afnan Albatati with the hardness measurements and Dr. Vahid Khademi for helpful discussions.

### ELECTRONIC SUPPLEMENTARY MATERIAL

The online version of this article (<https://doi.org/10.1007/s11837-019-03467-y>) contains supplementary material, which is available to authorized users.

### REFERENCES

1. S.L. Nyakana, J.C. Fanning, and R.R. Boyer, *J. Mater. Eng. Perform.* 14, 799 (2005).
2. R. Kolli and A. Devaraj, *Metals* 8, 506 (2018).
3. J.D. Cotton, R.D. Briggs, R.R. Boyer, S. Tamirisakandala, P. Russo, N. Shchetnikov, and J.C. Fanning, *JOM* 67, 1281 (2015).
4. R.R. Boyer and R.D. Briggs, *J. Mater. Eng. Perform.* 14, 681 (2005).
5. K. Faller and F.H.S. Froes, *JOM* 53, 27 (2001).
6. A.R. Morris, *Deslination* 31, 387 (1979).
7. M. Niinomi and C.J. Boehlert, in *Advances in Metallic Biomaterials*, chap. 8, vol. 3 (2015), pp. 179–213. [https://doi.org/10.1007/978-3-662-46836-4\\_8](https://doi.org/10.1007/978-3-662-46836-4_8).
8. F.H. Froes, H. Friedrich, J. Kiese, and D. Bergoint, *JOM* 56, 40 (2004).
9. W.F. Smith, *Structure and Properties of Engineering Alloys*, 2nd ed. (New York: McGraw-Hill, 1993), pp. 411–457.
10. G. Lütjering and J.C. Williams, *Titanium*, 2nd ed. (Berlin: Springer, 2007).
11. M. Ikeda, S. Komatsu, M. Ueda, and A. Suzuki, *Mater. Trans.* 45, 1566 (2004).
12. L.M. Gammon, R.D. Briggs, J.M. Packard, K.W. Batson, R. Boyer, and C.W. Domby, *ASM Handbook*, vol. 9, pp. 899–917. <https://doi.org/10.1361/asmhba0003779>.
13. A. Devaraj, D.E. Perea, J. Liu, L.M. Gordon, T.J. Prosa, P. Parikh, D.R. Diercks, S. Meher, R.P. Kolli, Y.S. Meng, and S. Thevuthasan, *Int. Mater. Rev.* 63, 68 (2018).
14. S. Nag, R. Banerjee, J.Y. Hwang, M. Harper, and H.L. Fraser, *Philos. Mag.* 89, 535 (2009).
15. E04 Committee, *Test Methods for Determining Average Grain Size* (ASTM International, n.d.).
16. W. Zhou, R.P. Apkarian, Z.L. Wang, and D. Joy, *Scanning Microscopy for Nanotechnology*, ed. W. Zhou and Z.L. Wang (New York, NY: Springer, 2006).
17. A. Devaraj, V.V. Joshi, A. Srivastava, S. Manandhar, V. Moxson, V.A. Duz, and C. Lavender, *Nat. Commun.* 7, 11176 (2016).
18. Y. Chang, A.J. Breen, Z. Tarzimoghdam, P. Kürnsteiner, H. Gardner, A. Ackerman, A. Radecka, P.A.J. Bagot, W. Lu, T. Li, E.A. Jägle, M. Herbig, L.T. Stephenson, M.P. Moody, D. Rugg, D. Dye, D. Ponge, D. Raabe, and B. Gault, *Acta Mater.* 150, 273 (2018).
19. R.P. Kolli, *Adv. Struct. Chem. Imaging* 3, 10 (2017). <https://doi.org/10.1186/s40679-017-0043-4>.
20. B. Gault, eds., *Atom Probe Microscopy* (New York: Springer, 2012).
21. J.M. Cairney, K. Rajan, D. Haley, B. Gault, P.A.J. Bagot, P.-P. Choi, P.J. Felfel, S.P. Ringer, R.K.W. Marceau, and M.P. Moody, *Ultramicroscopy* 159, 324 (2015).
22. A. Devaraj, T.C. Kaspar, S. Ramanan, S. Walvekar, M.E. Bowden, V. Shutthanandan, and R.J. Kurtz, *J. Appl. Phys.* 116, 193512 (2014).
23. A. Devaraj, M. Gu, R. Colby, P. Yan, C.M. Wang, J.M. Zheng, J. Xiao, A. Genc, J.G. Zhang, I. Belharouak, D. Wang, K. Amine, and S. Thevuthasan, *Nat. Commun.* 6, 8104 (2015).
24. M.P. Moody, L.T. Stephenson, A.V. Ceguerra, and S.P. Ringer, *Microsc. Res. Tech.* 71, 542 (2008).
25. D. Doraiswamy and S. Ankem, *Acta Mater.* 51, 1607 (2003).
26. S. Hanada and O. Izumi, *Metall. Trans. A* 18A, 265 (1987).
27. A. Jaworski and S. Ankem, *J. Mater. Eng. Perform.* 14, 755 (2005).
28. M. Ahmed, D. Wexler, G. Casillas, O.M. Ivasishin, and E.V. Pereloma, *Acta Mater.* 84, 124 (2015).
29. X.L. Wang, L. Li, W. Mei, W.L. Wang, and J. Sun, *Mater. Charact.* 107, 149 (2015).
30. R.P. Kolli, W.J. Joost, and S. Ankem, *JOM* 67, 1273 (2015).

**Publisher's Note** Springer Nature remains neutral with regard to jurisdictional claims in published maps and institutional affiliations.